PAPER

Check for updates

Enhanced photocatalytic organic dye removal by Ag-doped ZnO/GO nanocomposites: a combined experimental and DFT study

Kassa Belachew, [ID] [a] Newayemedhin A. Tegegne, [ID] *[a] Mesfin Abayneh Kebede, [ID] [b] Dinsefa Mensur Andoshe, [ID] [c] Qinfang Zhang [ID] [d] and Fekadu Gashaw Hone [ID] *[a]

In this work, Ag-doped ZnO/graphene oxide nanocomposites were synthesized by a co-precipitation technique and characterized systematically for their structural, optical, and photocatalytic properties. The XRD study confirmed the wurtzite phase of ZnO, and the successful incorporation of Ag and GO, besides an improvement in crystallinity and enlargement in crystallite size following composite formation. UV-Vis diffuse reflectance spectroscopy showed a reduced band gap from 3.20 eV (pure ZnO) to 3.00 eV (Ag–ZnO/GO), while photoluminescence spectra indicated the suppression of electron–hole recombination. Electron microscopy revealed that the Ag–ZnO nanoparticles are homogeneously distributed on the GO sheets. Under visible light, the photocatalytic efficiency of Ag–ZnO/GO towards Methylene Blue and Methyl Red reaches 99.98 ± 0.02 ($n = 3$)% and 92%, respectively, showing much higher efficiency compared to pure ZnO and Ag–ZnO. The DFT+U calculations show that the bandgap narrowed, while charge delocalization was improved, along with stronger adsorption of dye molecules on the Ag–ZnO/GO surface, as reflected by $E_{ads} = -1.49$ eV for MB and -1.61 eV for MR. The Mulliken charge analysis further confirmed the enhanced charge transfer $\Delta Q = -0.1573e$ for MB and $-0.1705e$ for MR because of the synergistic effect of Ag and GO. This study combines experimental and theoretical insights, showing that Ag–ZnO/GO nanocomposites possess efficient charge separation, superior light absorption, and excellent photocatalytic activity, thus presenting great promise for application in wastewater purification and environmental remediation.

1. Introduction

Large amounts of pollutants, such as dyes, organic solvents, and oils, are produced by industries and discharged into water resources. Water pollution is still one of the key concerns of society, which causes a shortage of fresh and clean water and is crucial for the sustainability of global pollution.[1–4] For this reason, new technologies for the photodegradation of organic contaminants have been created. The most efficient technique for treating wastewater is the photodegradation of dyes utilizing semiconductor materials assisted by the irradiation of sunlight with the reaction of hydroxyl radicals ($\bullet$OH).[5,6] It can completely oxidize organic colors at ambient temperature due to its high oxidation potential (2.8 V).[7]

Numerous research studies have examined modified metal oxides and hybrid nanostructures for the photocatalytic degradation of organic contaminants under light exposure. Varita Kumar *et al.*[8] revealed that a CuO/rGO nanocomposite degrades 98% of Eriochrome Black T in 80 minutes and eliminates 90% of Methyl Orange in 100 minutes. Similarly, Karina Bano *et al.*[9] reported that a $MnV_2O_6/BiVO_4$ heterojunction degraded 98–98.5% of Methylene Blue in just 6 minutes and 96.2% of Rhodamine B in 35 minutes. Mandvi *et al.*[10] used a NiO/Mn_3O_4 heterostructure to accomplish 93.6% degradation of Crystal Violet and 93.2% degradation of Rhodamine B in 80 minutes. Also, a CuO/PbO heterojunction that nearly totally degraded amoxicillin and malachite green was investigated by Karina Bano *et al.*[11]

ZnO-based nanocomposites have also shown high photocatalytic activity. In 120 minutes, ZnO nanoparticles[12] eliminated about 94% of Rhodamine B, and ZnO nanorods[13] removed 99.5% of Congo Red. Also 94% of tetracycline and 93% of ciprofloxacin were broken down in 50 minutes by a CuO/ZnO

[a] Department of Physics, Addis Ababa University, P. O. Box 1176, Addis Ababa, Ethiopia. E-mail: fekadu.gashaw@aau.edu.et

[b] Institute for Nanotechnology and Water Sustainability, College of Science, Engineering and Technology, University of South Africa, Florida Science Campus, Johannesburg, 1710, South Africa

[c] Adama Science and Technology, Department of Materials Science and Engineering, P.O. Box 1888, Adama, Ethiopia

[d] School of Materials Science and Engineering, Yancheng Institute of Technology, China

heterojunction[14]. Meanwhile, a GA-g-poly(MAA)/Ag nanocomposite[15] eliminated 92% of Methylene Blue and CTAB-coated CoO_4 nanoparticles[16] totally degraded Brilliant Yellow in 140 minutes.

In a study by Manisha Dagar et al.[17], a Ce/Ag/N-doped ZnO–MWCNT composite achieved 92.1% degradation of Congo Red and 87.5% of Methylene Blue within 80 minutes. SrO nanoparticles were also reported by Shimi et al.[18] to effectively degrade Methylene Blue and Rohilla et al.[19] also reported 98.1% removal of Methyl Orange using a $ZnO–SiO_2$ nanocomposite in 100 minutes. These results demonstrate that the photocatalytic degradation efficiency is consistently increased by metal incorporation, heterojunction formation, and coupling with carbon-based materials or secondary oxides.

Numerous investigations have demonstrated that ZnO is supposed to be a more effective photocatalyst than TiO_2.[20–22] In our previous study, we synthesized Cu, Co and Ni-doped ZnO NPs via Co-precipitation for the degradation of Methylene Blue and red dyes. In comparison with the pure materials and other dopants, Ni-doped ZnO has greater photocatalytic activity, which was confirmed by our DFT studies.[23] ZnO NPs doped with transition metals like Mn^{24} and Mg show better photocatalytic activity than pure ZnO for the removal of Methylene Blue, with around 99% and 96.6% removal, respectively. By altering the pH, Kumaresan et al.[25] used a hydrothermal method to synthesize various one (1D) and two dimensional (2D) ZnO nanostructures. The synthesized sample's photoactivity demonstrated that, following a 120-minute exposure to light irradiation, the two-dimensional structures resulted in 94% rhodamine B (RhB) dye degradation. A quick and easy method for preparing sea urchin-like three-dimensional (3D) ZnO nanostructures was recently developed by Kiriarachchi et al.[26] Superior photocatalytic effectiveness is demonstrated by the prepared ZnO nanostructures in the breakdown of typical organic dyes.[26] The size, shape, surface area, crystallinity, and stability of ZnO nanoparticles are all influenced by the conditions and procedures used during synthesis.[27,28]

Additionally, because of its enormous specific surface area and two-dimensional planar conjugated structure, graphene oxide (GO) offers a large scaffold for anchoring a variety of molecules.[29,30] Graphene-derived nanocomposites can be used effectively in photocatalytic, energy storage and photochemical processes due to their high surface area (about 2630 m^2 g^{-1}), and high electrical (106 S cm^{-1}) and thermal (5000 W m^{-1} K^{-1}) conductivities. Furthermore, the simplicity of functionalization gives graphene and its derivatives promisingly attractive properties.[31,32]

One of the main reasons limiting the effectiveness of ZnO-based photocatalysts is electron–hole recombination.[33] Consequently, a number of tactics have been used to reduce electron–hole recombination and increase ZnO's photocatalytic performance. Adding GO and metal nanoparticles to increase ZnO's photocatalytic activity is one of the effective strategies.[33,34] Qin et al.[35] have investigated the synergistic adsorption–degradation effects of Ag/ZnO/GO heterostructures for the removal of rhodamine B. They concluded that

Ag/ZnO/GO showed the best removal efficiency against RhB, with over 90% removal efficiency. While the addition of GO can successfully raise the light-harvesting capacity and dye adsorption, the doping of Ag into ZnO may effectively improve its photo-degradation activity.

A. F. Nathir et al.[1] have studied the photocatalytic activity of Ag metal-embedded graphene oxide/zinc oxide nanocomposites for the degradation of Methylene Blue dyes. After 40 minutes of exposure to sunlight, the GO–ZnO–Ag nanocomposites achieved 100% effectiveness in MB removal. For the photodegradation of organic dyes in industrial wastewater, the GO–ZnO–Ag nanocomposite thus has the potential to be an effective versatile photocatalyst. Al-Mamun, Md Rashid et al.[36] prepared a novel and highly efficient Ag and GO/ZnO nano photocatalyst for the degradation of Methylene Blue dye under UV irradiation and achieved 97% degradation efficiency of Methylene Blue.

Because of its hydrophilic nature, aromatic structure, and high stability, Methylene Blue photodegradation proceeds via oxidation after an initial reduction.[37] In addition, anionic and hydrophobic Methyl Red dye, which is sparingly soluble in water, is also another pollutant that dissolves well in polar organic solvents like methanol and ethanol.[38] Its solubility is higher under alkaline conditions owing to ionization of the carboxylic group, which also affects its optical and photocatalytic properties.[38,39] Although metal-doped ZnO/GO photocatalysts have been widely investigated and exhibit efficient dye degradation, the underlying adsorption energy characteristics and electronic mechanisms governing this performance are rarely explained with combined experimental and DFT insights. To bridge these gaps, we tested Ag:ZnO/GO nanocomposites with Methylene Blue and Methyl Red. We have identified that Ag acts as an efficient electron mediator, whereas GO offers fast charge-transport pathways, both of which synergistically enhance light absorption, charge separation, and ROS generation. The electronic origin of such an enhancement has been further explained through complementary DFT studies, including band structure, DOS, adsorption energy and Mulliken charge calculations. Overall, this work offers a better insight into atomic-level photocatalytic mechanisms in metal-doped ZnO/GO systems and presents high pollutant-decolorization efficiency for Ag:ZnO/GO nanocomposites.

2. Materials and methodology

2.1. Materials

The main chemicals and reagents used in the laboratory were zinc acetate dihydrate ($Zn(CH_3COO)_2 \cdot 2H_2O$), silver nitrate ($AgNO_3$), sodium hydroxide (NaOH), acetone (C_3H_6O), graphite, sulfuric acid (H_2SO_4), potassium permanganate ($KMnO_4$), hydrogen peroxide (H_2O_2), hydrochloric acid (HCl), Methyl Red dye ($C_{15}H_{15}N_3O_2$) and Methylene Blue ($C_{16}H_{18}ClN_3S$).

2.2. Experimental methods

2.2.1. Preparation of graphene oxide (GO). Graphene oxide (GO) was prepared from graphite powder through the modified

Hummers' method. A mixture of 50 mL of concentrated H_2SO_4 was cooled in an ice bath and maintained at temperatures below 5 °C, then 2 g of graphite powder was added slowly. 6 g of potassium permanganate solution was slowly added while the temperature was maintained below 20 °C with constant stirring for a period of 3 hours. The mixture was further heated to 35–40 °C and stirred for 2 hours to form a thick paste. Later, 100 mL of deionized water was slowly added to the mixture, accompanied by keeping the temperature below 50 °C. After some time, the mixture color changes to dark brown, which indicates the formation of graphene oxide. Again, 100 ml of DI water was added to complete oxidation. After that, 6 mL of hydrogen peroxide solution was added to stop the reaction, turning the mixture bright yellow. The resulting mixture was centrifuged at 3000 rpm for 20–30 minutes after it was washed with 100 mL of HCl in 900 mL deionized water to eliminate metal ions to the supernatant. To neutralize the pH, it was washed with deionized water through centrifugation at higher speeds of 3000 rpm for 30 minutes for 5–6 cycles. Finally, the prepared graphene oxide sample was dried in a vacuum oven at 50 °C to yield a dark-brown powder.

2.2.2. Synthesis of Ag-doped ZnO/GO nanocomposites *via* a co-precipitation method. For the synthesis of the Ag-doped ZnO/GO nanocomposites, zinc acetate dihydrate ($Zn(CH_3COO)_2$· $2H_2O$) was employed as the major precursor. 8.7 g of zinc acetate was dissolved in 200 mL of deionized for 1 h at room temperature until a clear transparent solution was created. The appropriate amount of silver nitrate ($AgNO_3$) was added to the clear solution and stirred for 1 h at room temperature to make the solution homogeneous. A graphene oxide (GO) dispersion was separately prepared with intense stirring for 30 minutes. Then, the prepared zinc acetate and silver nitrate homogeneous solution was added to the GO suspension. This mixture solution was treated with 1 M-NaOH solution in small portions until it reached pH-10 or a milky solution formed. The solution mixture was stirred for 2 hours while raising the temperature to 85 °C to complete the chemical reaction. The precipitate was centrifuged at 3000 rpm to separate it from the solution mixture, washed with deionized water and ethanol 6 times to remove ions, and dried in an oven at 80 °C for 12 hours to dry the material. Finally, the powder was calcined in an oven at 400 °C for 2 hours and ready for the proposed study.

2.2.3. Computational methods. DFT+U calculations were employed to determine the localized nature of Zn 3d and Ag 4d electrons. Hubbard U values were selected based on the established literature to improve the electronic structure or to correct Zn 3d localization effects. The computational model represents an idealized hetero-interface designed to capture qualitative electronic and charge redistribution trends rather than precise quantitative predictions. Hubbard U values of 10[40,41] and 6 eV[42] were added as U corrections to Zn and Ag atoms, respectively. The Zn_8O_8 wurtzite structure was treated with a hexagonal lattice (ibrav = 4), whereas an ideal planar Ag/ZnO/GO system is treated with (ibrav = 0). A wavefunction cutoff of 50 Ry with a charge density of 500 Ry as well as a k-point mesh of $4 \times 4 \times 4$ and $2 \times 2 \times 2$ Monkhorst–Pack grid divisions was used to treat the pure and hybrid systems, respectively. Optimization of the structures involved the BFGS algorithm under high accuracy in energies as well as forces.

2.3. Characterization techniques

Structure analysis of the prepared materials was done by X-ray diffraction (XRD) (Rigaku RINT-2500, Cu Kα, λ = 1.54 Å, 40 kV, and 20 mA). A fluorescence spectrophotometer (Hitachi F-2500) was used to measure photoluminescence spectra of the materials. Morphology and elemental composition were studied by an EDX-equipped FESEM (Hitachi SU8000 Type II), while SEM (JeolJSM-7500) and TEM provided detailed microstructural and particle size information. Diffuse reflectance spectroscopy (DRS) was applied to study the optical absorption properties and to estimate the bandgap energies required for photocatalytic activity.

3. Results and discussion

3.1. XRD analysis

Fig. 1 shows the XRD patterns of the ZnO, Ag:ZnO and Ag:ZnO/GO nanocomposites. The XRD pattern of ZnO gives sharp and intense diffraction peaks at 31.90, 34.50, 36.40, 47.70, 56.70, 63.00, 66.60, 68.20, and 69.30 for the corresponding planes (100), (002), (101), (102), (110), (103), (200), (112), and (201), showing the crystalline nature of ZnO, which agrees with JCPDS card number 043-0002 and exhibits the wurtzite crystal structure[23] of the material with no additional peaks.

Incorporation of Ag into ZnO did not alter the wurtzite diffraction pattern of pure ZnO, confirming the successful formation of Ag clusters on the ZnO surface, rather than substitution into the lattice. In the Ag–ZnO/GO composite, no characteristic diffraction peaks of GO were detected, which is attributed to its low loading and the exfoliated nature of the GO sheets. The appearance of Ag-related peaks together with the unchanged wurtzite structure of ZnO indicates that neither Ag
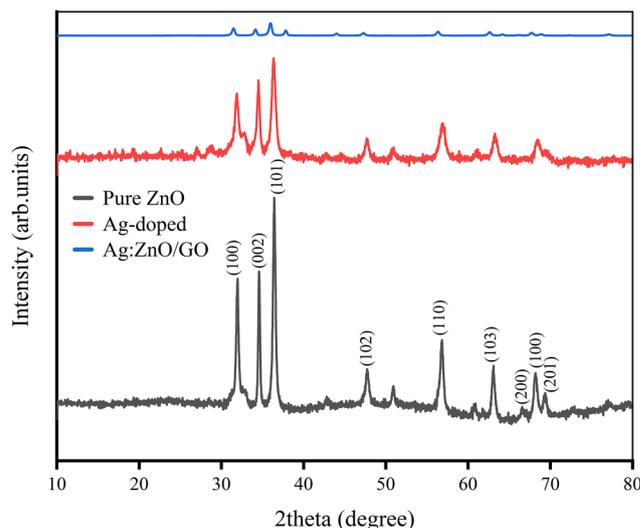

Fig. 1 XRD patterns of the ZnO, Ag:ZnO and Ag:ZnO/GO nanocomposite.

nor GO disturbs the crystal phase of ZnO. The crystallite size in the case of Ag–ZnO/GO was larger than that of pure ZnO, indicating the enhanced crystal growth, which may be due to Ag serving as nucleation sites and better interfacial coupling with GO. This confirms that the Ag–ZnO/GO nanocomposite was formed successfully without any impurity phases. The average crystalline size of ZnO, Ag:ZnO and Ag:ZnO/GO was calculated by using the Debye Scherrer equation[43] for the (101) crystal plane.

$$D = \frac{K\lambda}{\beta \cos\theta} \tag{1}$$

Here, λ is the X-ray wavelength, K is a shape factor with no dimensions, β is the line broadening at full width half maximum intensity and θ gives the value of Bragg angle. The interplanar spacing for the ZnO nanoparticles was measured by using the Bragg formula for X-ray diffraction.[23]

$$n\lambda = 2d \sin\theta \tag{2}$$

where λ is the X-ray wavelength ($\lambda = 1.54178$ Å), n is a positive digit having value equal to 1 and θ is the angular position of the hkl reflection.

XRD analysis of pure-ZnO, Ag:ZnO and Ag:ZnO/GO NPs reveals that structural variation plays an important role in photocatalytic activity. Pure ZnO has a crystallite size of 10.92 nm and a dislocation density of 83.8×10^{-4}, while Ag doping reduces the crystallite size to 10.50 nm and the dislocation density to 89.6×10^{-4} with minimal decrease in crystallinity. This increase in surface area to volume ratio with the enhanced surface[44] of the Ag nanoparticles thereby improves the photocatalytic properties (Table 1).

As expected, Ag:ZnO/GO shows a significantly higher crystallite size of 36.28 nm with increased crystallinity and reduced lattice defects, and the GO sheets serve as a supporting matrix that facilitates charge transport.[45]

Compared to pure-ZnO, the higher crystallite size Ag–ZnO/GO nanocomposite achieved much higher photocatalytic activity due to the formation of a heterojunction, as well as efficient charge transfer.[46] The crystallite size obtained from XRD ($\sim$36 nm) represents the primary crystalline domains of ZnO, determined from the broadening of the diffraction peaks using the Scherrer equation.[47]

3.2. UV-Vis diffuse reflectance spectra (DRS)

The optical absorption behavior of the composites was examined using UV-Vis diffuse reflectance spectroscopy. Because heterostructured composites exhibit multiple electronic
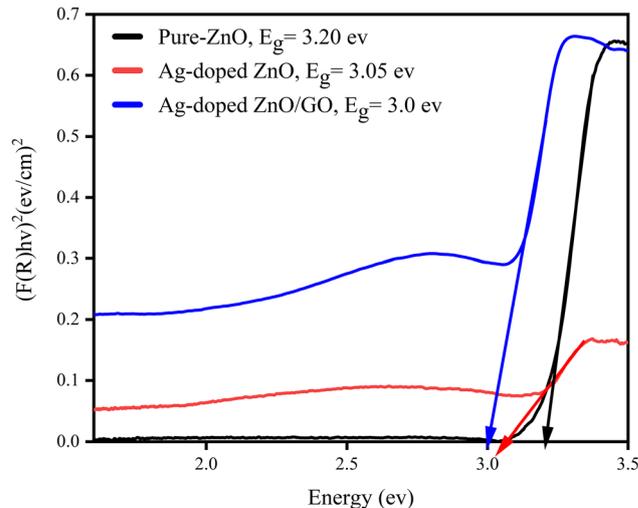

Fig. 2 Optical energy band gap of the ZnO, Ag:ZnO and Ag:ZnO/GO nanocomposite.

transitions, the estimated bandgap values should be interpreted comparatively. Nevertheless, the progressive red-shift and apparent bandgap narrowing upon Ag doping and GO incorporation clearly indicate enhanced visible-light absorption, consistent with interfacial electronic interactions and defect-mediated states.[36,48] The UV-Vis diffuse reflectance spectra (see Fig. 2) of the pure ZnO, Ag-doped ZnO, and Ag-doped ZnO/GO composites evidenced the difference in their optical properties through which their expected photocatalytic activity was enhanced. The Kubelka–Munk relation is used to approximate the optical band gap:

$$F(R) = \frac{k}{s} = \frac{(1 - R)^2}{2R} \tag{3}$$

Considering a direct band gap transition, the band gap energies of the samples were calculated by graphing $(\alpha h\nu)^2$ against $h\nu$[49] with reference to Fig. 2's absorption spectra. Pure ZnO was found to possess an optical bandgap of 3.20 eV, which dropped to 3.05 eV after doping with Ag and further down to 3.00 eV for the Ag-doped ZnO/GO composites.[45] Related studies reported similar results.[45,48,50]

3.3. Photoluminescence (PL) spectra

The PL spectra of the samples in Fig. 3 show a near-band-edge emission centered at $\sim$395–405 nm and a visible band from 430 to 550 nm, associated with excitonic recombination and defect-related states in ZnO, respectively.[51] All materials show low PL intensities, implying less radiative recombination of charge carriers. The doping of Ag causes a decrease in PL intensity, implying a further decrease in recombination by electron trapping. Also, Ag:ZnO/GO shows the strongest quenching of PL, revealing the most efficient charge separation and transfer, attributable to the synergistic effect of Ag and graphene oxide.[51,52]

Table 1 Calculated crystallite size and other parameters

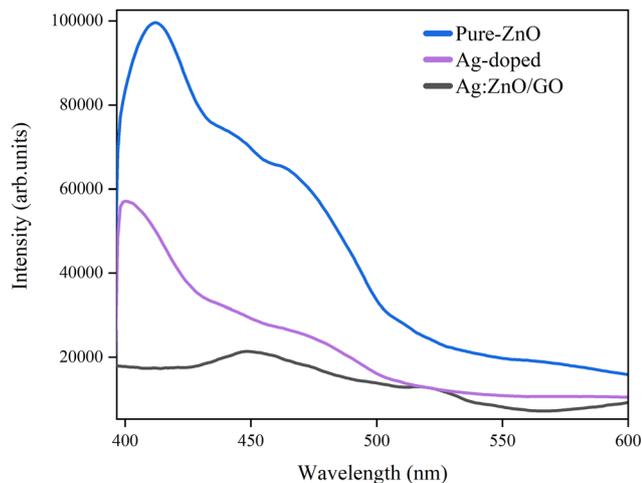| Sample	Crystal size (D)	Dislocation density (δ) (kJ m^{-3})	ε (line^{-2} (nm)$^{-4}$) ($\times 10^{-4}$)	Lattice parameter	
				a (Å)	c (Å)
Pure-ZnO	10.92	83.8×10^{-4}	16.20	3.2208	5.1824
Ag:ZnO	10.50	89.6×10^{-4}	15.20	3.2408	5.1923
Ag:ZnO/GO	36.28	76×10^{-4}	17.30	3.2783	5.2466

Fig. 3 PL emission spectra of undoped and Ag-doped ZnO/GO nanocomposites.

3.4. The EDX, SEM and TEM analyses

The EDX spectra of the pure ZnO and Ag–ZnO/GO nanocomposites are displayed in Fig. 4(a and b), respectively. The presence of a small C peak in the pure ZnO spectrum is said to be attributed to the carbon tape or the remaining organic species, whereas Zn and O validate the successful formation of ZnO. For Ag–ZnO/GO, there is the presence of extra peaks of Ag and enhanced signals of C, suggesting the successful integration of silver and the presence of the graphene oxide matrix. These results all validate the formation of a Ag–ZnO/GO composite and successful integration of Ag and GO into the ZnO structure.[1,53]

The SEM images of the synthesized ZnO, Ag:ZnO, and Ag:ZnO/GO nanocomposites are shown in Fig. 5(a–c), respectively. The corresponding particle size distributions of the samples are also shown in Fig. 5(d–f), respectively. From the SEM image (Fig. 5a), 3D irregular ZnO particles are clearly

shown.[54,55] The average particle size is approximately 225 nm (Fig. 5d).[56] After Ag doping (Fig. 5b), the ZnO particles become more dense and packed.[57] This leads to a slight increase in the average particle size to 375 nm (Fig. 5e). The Ag doping significantly improves the charge separation and electron mobility. In the Ag:ZnO/GO composite (Fig. 5c), Ag:ZnO nanoparticles are homogenously dispersed on the wrinkle-covered 2D GO sheets. This leads to the formation of a 3D hierarchical porous structure.[55] The average particle size again significantly increases to 550 nm (Fig. 5f) as the Ag:ZnO nanoparticles tend to form clusters at the surface of the GO sheets. In the Ag:ZnO/GO composite, the incorporation of GO establishes an excellent conductive pathway to pass the photogenerated electrons quickly. This assists in efficient charge transfer and suppresses the recombination of photoexcited carriers. Thus, the photocatalytic activities increase progressively from the ZnO to Ag:ZnO photocatalyst and finally to the Ag:ZnO/GO photocatalyst.[58]

Fig. 6(a–c) represents the transmission electron microscopy (TEM) images of the pure ZnO, Ag-doped ZnO, and Ag-doped ZnO/GO nanocomposites, respectively. As observed in Fig. 6(a), pure ZnO nanoparticles display a hexagonal to quasi-spherical morphology with an average particle size of 64.40 nm.[59] The nanoparticles were fairly monodisperse but tended to form agglomerates because of their large surface energy. In Fig. 6(b), the Ag-doped ZnO nanoparticles exhibit slightly smaller and non-uniform shapes, with particle sizes of 24.30 nm.[60] The darker spots indicate Ag nanoparticles spread around the ZnO surface. The addition of Ag alters the ZnO lattice and promotes visible-light absorption by the surface plasmon resonance (SPR) of silver.

In Fig. 6(c), nanoparticles are uniformly distributed and tightly attached on the thin, partially wrinkled graphene oxide (GO) sheets in the Ag-doped ZnO/GO nanocomposite. The GO network acts as a conductive matrix that prevents nanoparticle agglomeration and facilitates efficient charge transfer between
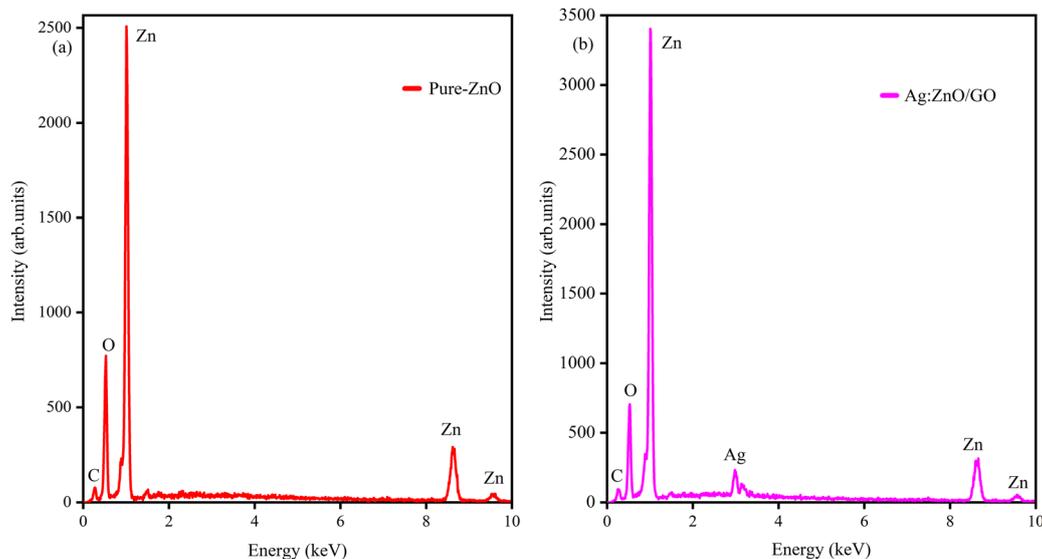

Fig. 4 The representative EDX spectra of the (a) undoped ZnO and (b) Ag-doped ZnO/GO nanocomposites.
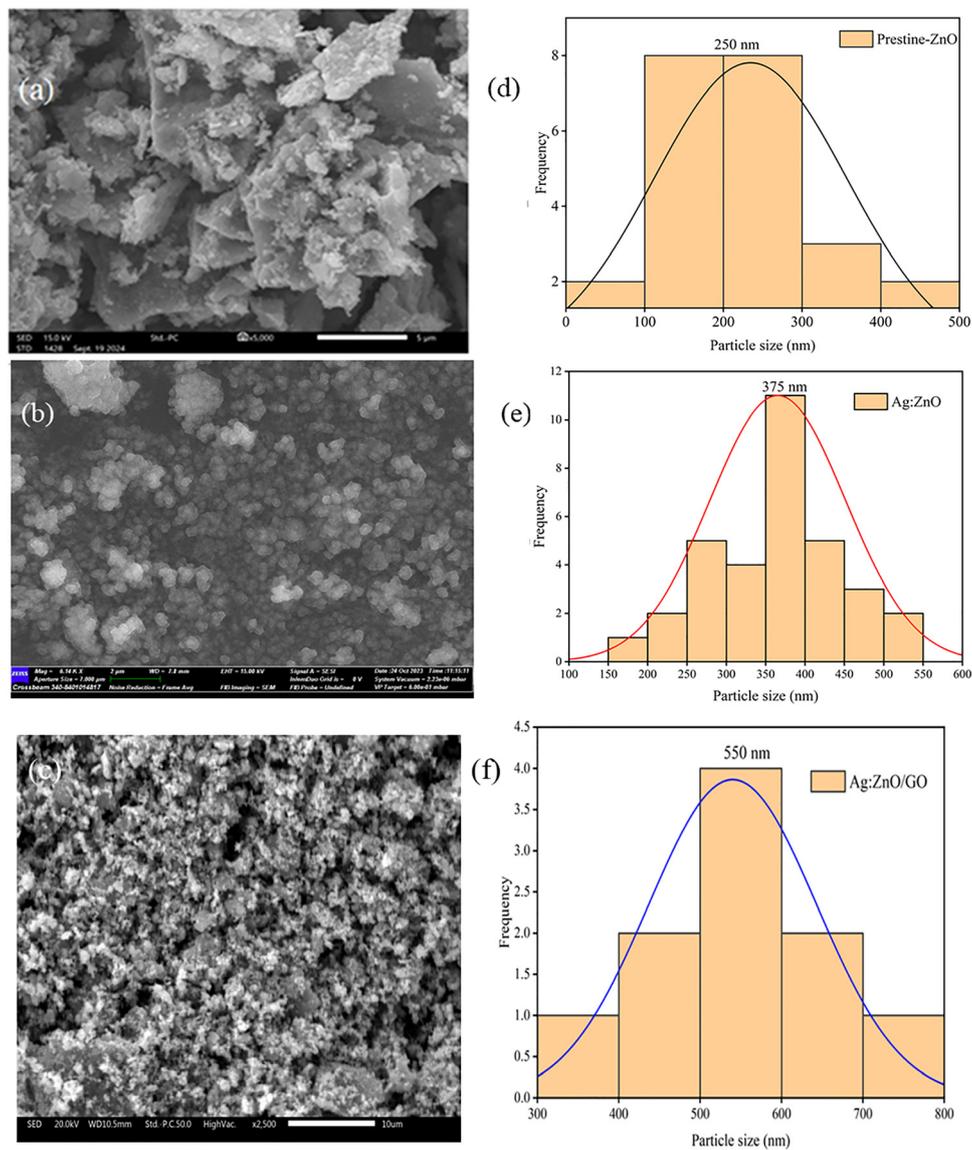
Fig. 5 The SEM micrograph images and Gaussian distribution histogram diagram pair for (a) and (d) pristine ZnO, (b) and (e) Ag-doped ZnO, and (c) and (f) Ag-doped ZnO/GO nanocomposites.
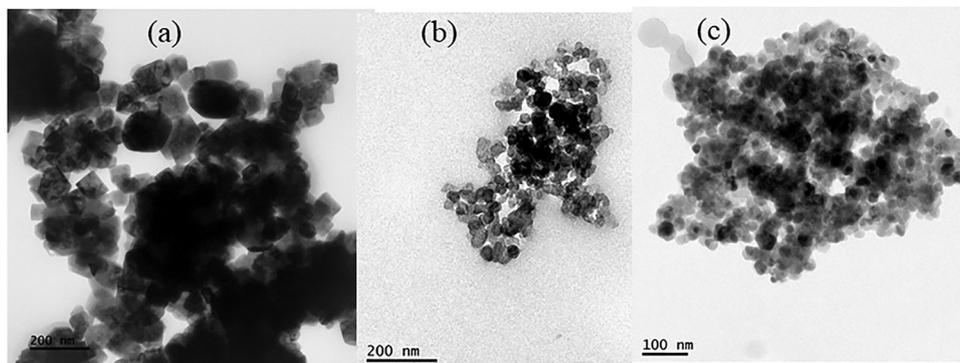

Fig. 6 TEM images of (a) pristine ZnO, (b) Ag-doped ZnO, and (c) Ag-doped ZnO/GO nanocomposites.

components.[60,61] Relatively smaller average sizes of the particles were found (around ~24.70 nm), with a close contact of Ag, ZnO, and GO that results in various heterojunction interfaces that facilitate fast electron transfer from ZnO to GO, where Ag is used as a mediator of electron transfer.[61] This synergistic structure suppresses recombination more effectively than in the individual components, resulting in enhanced light absorption, improved charge separation, and higher surface reactivity.

The particle sizes obtained from SEM and TEM reflect different structural levels of the Ag–ZnO/GO nanocomposites. SEM particle size (550 nm) reveals secondary agglomerates formed through the aggregation of multiple primary particles.[62,63] TEM with higher resolution directly visualizes the primary ZnO[47] nanoparticles anchored on the GO sheets. Therefore, the difference between the XRD crystallite size and the SEM particle size reflects the formation of larger agglomerates from smaller primary crystallites, rather than an inconsistency between the two measurements.

3.5. Photocatalytic activity

Photocatalytic tests were carried out using a 450 W UV reactor and water cooling system. The lamp-solution distance of about 4–6 cm provided an estimated 180 mW cm^{-2}. The reaction mixture consisted of 100 mL of dye solution (MB, 15 ppm or MR, 30 ppm) and 0.065 g of photocatalyst (ZnO or doped ZnO/GO nanocomposite).

Prior to visible-light irradiation, the suspension was stirred at 500 rpm with a magnetic stirrer in the dark for 60 min[46] at room temperature. This helps to establish better adsorption–desorption equilibrium between the dye molecules and the photocatalyst surface. Pure ZnO was first tested at pH 4 and pH 10 to determine the optimal conditions. The control experiments conducted under light-only and dark (catalyst-only) conditions showed negligible degradation, confirming that the activity of Ag–ZnO/GO arises from photocatalysis. All further experiments were carried out at pH 10, with 5 mL samples taken every 20 minutes during visible light irradiation. The photocatalyst was separated via centrifugation, and the concentration of the remaining dye was determined using a
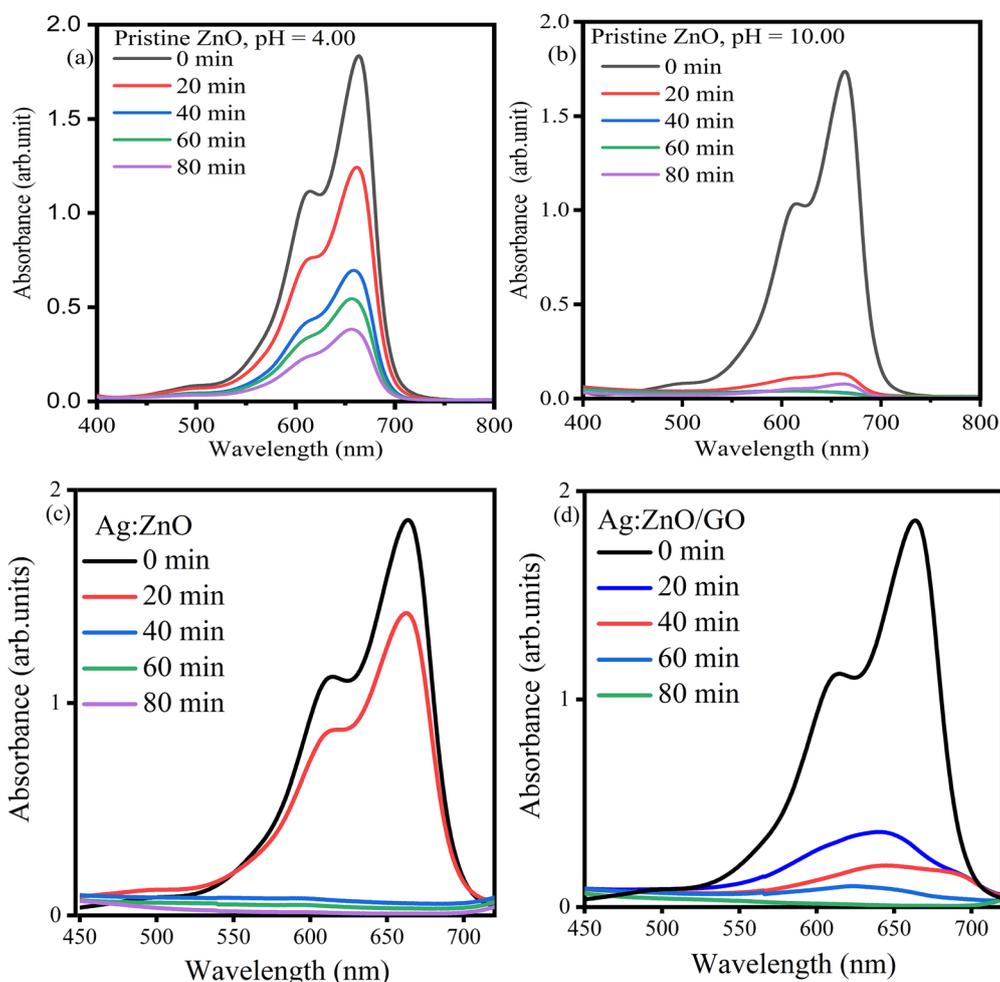

Fig. 7 Methylene Blue dye UV-Vis absorption spectra at various time intervals with (a) pristine ZnO at pH-4, (b) pristine ZnO at pH-10, (c) Ag-doped ZnO at pH-10 and (d) Ag-doped ZnO/GO at pH-10.

UV-Vis spectrophotometer by recording the characteristic absorption spectra.

The photocatalytic performances of the pure ZnO, Ag-doped ZnO, and Ag-doped ZnO/GO nanocomposites were assessed for MB/MR dye removal through visible-light irradiation, as shown in Fig. 7(a–d) and 8(a–d). During the photocatalytic dye removal/decolorization process the absorbance spectrum of MB/MR (664/540 nm) shows a decreasing pattern in the time scale of 0–80 minutes, indicating a reduction in the intensity of the primary absorbance peak associated with the typical wavelength of MB/MR. This depicts the removal of the MB/MR molecules with irradiance time. As indicated in Fig. 7(a and b), we analyzed the photocatalytic activity of pure ZnO at pH 4 and pH 10 to select better pH for the removal of the dyes. At pH 10, the surface of ZnO is negatively charged due to the deprotonating of hydroxide groups, favoring strong electrostatic repulsion in the direction of the positive charges of MB molecules, thus improving the efficiency of photocatalytic dye removal/decolorization.[64] On the other hand, at pH 4, the positive charge of the surface of ZnO electrostatically repels the positive charge of the MB molecules, with reduced adsorption as well as slow

removal.[64] Therefore, the removal efficiency of pure ZnO was determined to be 79.4% at pH 4 and recorded as 98.3% at pH 10 after irradiance in the visible region for 80 min, validating that the alkaline environment strongly favors photocatalytic dye removal of MB.

The absorbance spectra in Fig. 7(c) indicate that the Ag-doped ZnO nanoparticles also displayed a continuous decrease in MB absorbance with increased irradiation time, implying their effective photocatalytic activity. The results from the earlier PL confirmed that electron–hole recombination is suppressed by Ag doping by forming Schottky junctions, thereby promoting charge separation. The photocatalytic efficiency of Ag:ZnO (99.2%) was slightly increased compared to pure ZnO (98.3%). The Ag-doped ZnO/GO nanocomposite (Fig. 7d) demonstrated a significant enhancement in photocatalytic activity, with a rapid and high decolorization efficiency of the MB within 80 minutes of light illumination. Because of the synergistic effects of Ag and GO, Ag-doped ZnO/GO achieved high efficiency of MB decolorization of 99.98 ± 0.02 ($n = 3$)%. The results indicate that while Ag doping enhances charge-carrier dynamics, the GO–Ag–ZnO composite provides a
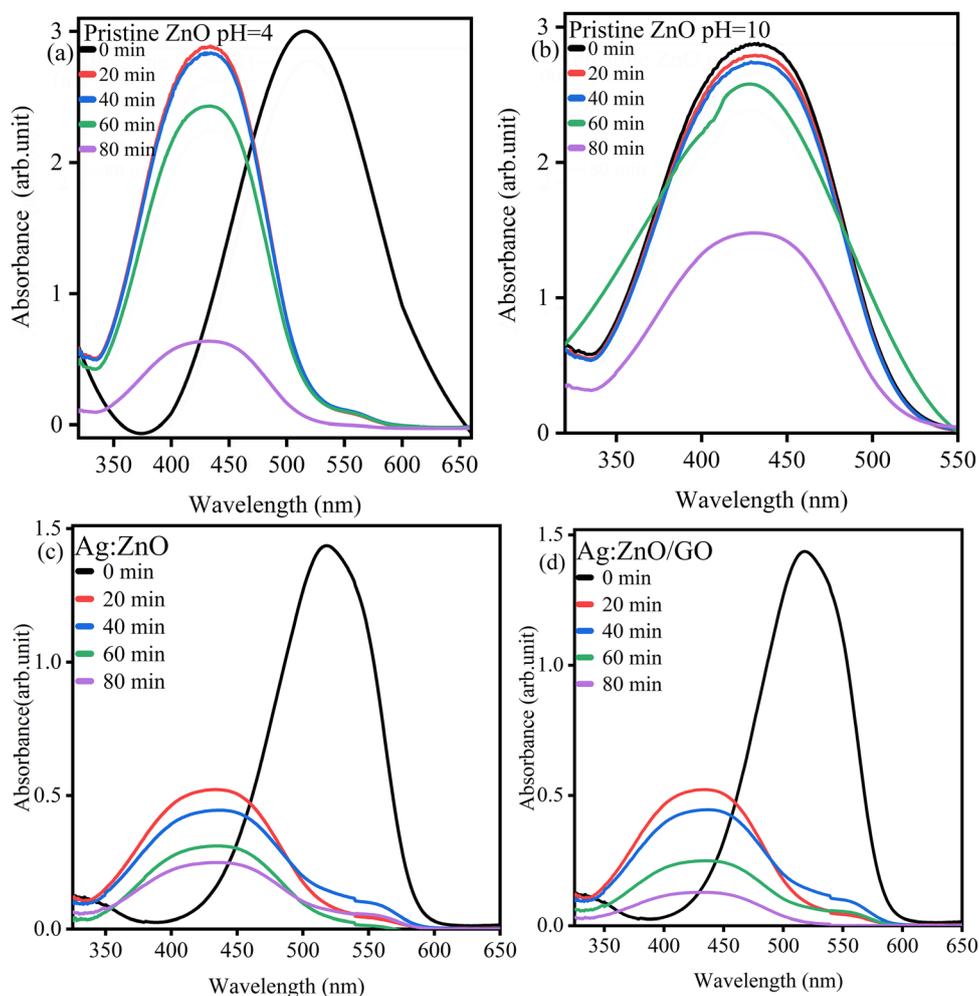

Fig. 8   Methyl red dye UV-Vis absorption at various time intervals with (a) pristine ZnO at pH-4, (b) pristine ZnO at pH-10, (c) Ag-doped ZnO at pH-4 and (d) Ag-doped ZnO/GO at pH-4.

synergistic effect, optimizing visible-light absorption and electron transport, making it the most effective photocatalyst for MB removal.[35,61]

Fig. 8(a–d) shows the decolorization efficiency of the materials for Methyl Red dye. It depicts that Methyl Red degraded fast at pH 4. Similarly, the Ag–ZnO/GO nanocomposite shows better decolorization efficiency of Methyl Red (92%) than the Ag-doped ZnO (83%) and pure ZnO (80.4) at pH 4 in the same measurement trend as Methylene Blue before. Ag promotes ZnO by increasing its ability to trap more light and facilitating easy excitation of electrons and graphene oxide (GO) acts as a fast track that rapidly transfers these electrons before recombination. Essentially, the combination of Ag and GO makes ZnO more active.

The short-term cycling stability over five cycles and reusability of the synthesized photocatalysts were assessed by choosing the Ag–ZnO/GO nanocomposite that displayed the optimal value of photocatalytic effectiveness (99.98 ± 0.02 (n = 3)%) in the decolorization of Methylene Blue (MB) compared with pure ZnO (98.3%) and Ag–ZnO (99.20%). The recyclability experiment was carried out by conducting five successive decolorization cycles under visible-light irradiance, as depicted in Fig. 9(a). After each cycle, the photocatalyst was separated by centrifugation at 4000 rpm for 20 min, thoroughly washed with a mixture of distilled water and ethanol in a volume ratio of 1 : 3, and gently dried before reuse.[65]

At the beginning, the Ag–ZnO/GO nanocomposite showed almost full decolorization of MB in 80 minutes. As the number of cycles increased, there was a gradual decline in the value of photocatalytic effectiveness, due to negligible losses of mass of the photocatalyst in the process of washing and recovery, as well as partial trapping of the surface through the adsorption of residuals of organic intermediate products. Even after five cycles, Ag–ZnO/GO still achieved over 93% decolorization efficiency, indicating excellent chemical stability and good reusability. The stable interface interaction of Ag, ZnO, and GO is responsible for the better reusability of the Ag–ZnO/GO photocatalyst, and it ensures structural stability and charge transport channels for cyclic use. The GO sheets also suppress the aggregation of the nanoparticles and maintain the active sites of the surface, thereby enabling long-term cycles with photocatalytic activities.[61,66] Although the recyclability results demonstrate good short-term stability of the Ag–ZnO/GO photocatalyst, quantitative evaluation of possible Ag leaching using techniques such as Inductively Coupled Plasma Optical Emission Spectroscopy would be necessary to fully assess long-term environmental stability.

Radical trapping experiments provide supportive evidence of reactive species involved in reactions. Reactive species trapping experiments were carried out using ascorbic acid (AA), dimethyl sulfoxide (DMSO), isopropyl alcohol (IPA), and ethylenediaminetetraacetic acid (EDTA) as scavengers for superoxide radicals ($^{\bullet}O_2^-$), electrons (e^-), hydroxyl radicals ($^{\bullet}OH$), and photogenerated holes (h^+), respectively.[44] Among the tested photocatalysts, Ag-doped ZnO/GO showed the best photocatalytic activity for the photocatalytic dye removal of Methylene Blue (MB) and was

chosen for the scavenger experiment. From Fig. 9b, it is clear that the Ag-doped ZnO/GO catalyst showed a photocatalytic dye removal efficiency of ≈99.98 ± 0.02 (n = 3)% for MB photocatalytic dye removal without the use of scavengers. However, the photocatalytic dye removal efficiency was found to reduce to ≈92.5%, 67%, 38.4%, and 25.7% with the use of DMSO, AA, EDTA, and IPA, respectively. The pronounced suppression of photocatalytic activity in the presence of IPA and EDTA strongly suggests that hydroxyl radicals ($^{\bullet}OH$) and photogenerated holes (h^+) play dominant roles in the photocatalytic degradation of MB over the Ag–ZnO/GO catalyst (Table 2).

With a fixed dye concentration, the photocatalytic dye removal/decolorization kinetics were analyzed using the pseudo-first-order expression, $\ln(C_0/C_t) = kt$. According to the Langmuir–Hinshelwood model, the reaction rate is

$$r = -\frac{\mathrm{d}c}{\mathrm{d}t} = k_\mathrm{r} KC/(1 + KC) \qquad (4)$$

where r is the decolorization rate, k_r is the reaction constant, K is the adsorption coefficient of the reactant, and C is the dye concentration.

For the low initial dye concentrations used (15 mg L^{-1} for MB and 30 mg L^{-1} for MR), the term KC is small, and the rate simplifies to pseudo-first-order behavior.[67,68] Linear fitting was performed over the 0–80 min irradiation period. Slight deviations at high conversion (>70–80%) are attributed to reduced dye concentration and diffusion limitations. The obtained k values are compared with recent ZnO-based photocatalysts in Table 3.
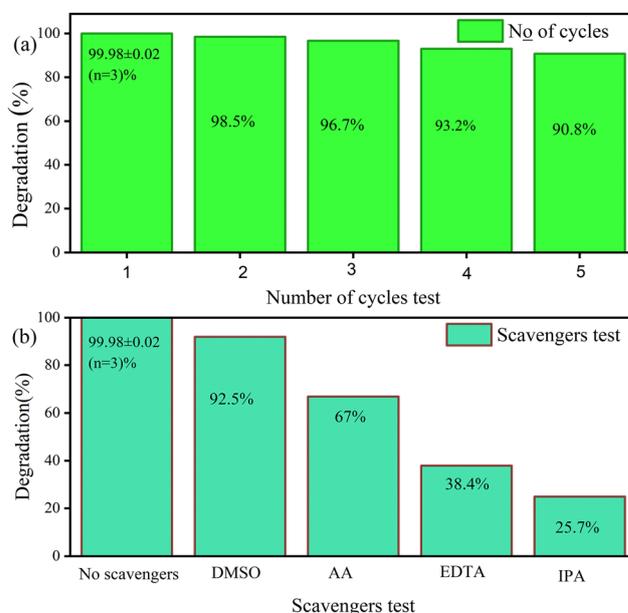

Fig. 9 (a) Reusability of the Ag-doped ZnO/GO photocatalyst for MB photocatalytic dye removal/decolorization, and (b) scavenger effects on MB photocatalytic dye removal/decolorization by using the Ag-doped ZnO/GO photocatalyst.

Table 2 Efficiency of decolorization of undoped and Ag-doped ZnO/GO NPs

Time (min)	ZnO	Ag-doped ZnO	Ag-doped ZnO/GO
Methylene Blue dye decolorization (%) by various photocatalysts			
0	0	0	0.00 ± 0.00 ($n = 3$)
20	92.3	23	79.83 ± 1.61 ($n = 3$)
40	95.4	96.7	90.56 ± 1.43 ($n = 3$)
60	98.1	98.3	96.20 ± 0.72 ($n = 3$)
80	98.3	98.9	99.98 ± 0.02 ($n = 3$)
Methyl Red dye decolorization (%) by various photocatalysts			
0	0	0	0
20	12.1	61	63
40	13.7	69	71
60	26.2	78	83
80	80.4	83	92

The rate constant is provided from pseudo-first-order kinetics by using the formula:[69]

$$\ln\left(\frac{C_0}{C_t}\right) = kt \tag{5}$$

where k is the first order rate constant and t is irradiation time.

From Fig. 10a and b, k is found to be 5.0×10^{-2} and 5.57×10^{-2} min^{-1} for MB in undoped and Ag-doped ZnO/GO NPs, respectively. Similarly, k is 1.63×10^{-2} and 2.5×10^{-2} min^{-1} for MR, respectively. When compared to undoped ZnO NPs, Ag-doped ZnO/GO NPs have demonstrated a much greater photocatalytic dye removal/decolorization rate constant (k) value. The large coefficients of determination ($R^2 = 0.959$ for MB and $R^2 = 0.956$ for MR) suggest an excellent fit for the pseudo-first-order kinetic model for the photocatalytic activity of Ag-doped ZnO/GO. This shows that the reaction is occurring at a constant rate and thus shows effective photocatalytic activity. In general, the Ag–ZnO/GO nanocomposite achieved 92% decolorization efficiency for Methyl Red (MR). This figure is significantly higher than that of Ag-doped ZnO ($83\% \pm 0.03$) and pure ZnO ($80.4\% \pm 0.02$) at pH 4. The decolorization efficiency for MB was near perfect (99.98 ± 0.02 ($n = 3$)%).

To check the reproducibility, the photocatalytic decolorization tests were carried out three times. The decolorization efficiencies were 99.96%, 99.99%, and 99.99%, resulting in an average of $99.98 \pm 0.02\%$ ($n = 3$) in Fig. 10(e), validating excellent photocatalytic performance. Even if the experimental results demonstrate efficient photocatalytic dye removal, the adsorption characteristics and electronic mechanisms underlying this performance remain unclear. Hence, DFT calculations were employed to investigate dye adsorption, charge transfer, and electronic structure modification in the Ag:ZnO/GO system.

3.6. DFT calculations

To investigate the structural, electronic, and adsorption properties of pristine ZnO and the Ag–ZnO/GO hybrid system, all calculations were carried out using density functional theory with Hubbard U corrections (DFT+U) by using the Quantum ESPRESSO package. For the pure ZnO cluster, a highly stable,[76] computationally traceable and frequently used Zn_8O_8[77,78] cluster model was chosen to represent the hexagonal wurtzite structure, with optimized lattice parameters of celldm (1) = 6.21 and celldm (3) = 1.61. Solvent and surface terminations can influence charge transfer. In this work, DFT calculations were performed under vacuum with fully relaxed structures, capturing the fundamental adsorption and charge-transfer behavior. So, without explicit solvent or surface reconstruction, the calculated results represent idealized qualitative trends.

To accurately describe the strongly correlated electrons, the Brillouin zone was sampled using a $4 \times 4 \times 4$ Monkhorst–Pack k-point grid for self-consistent calculations, and a denser $14 \times 14 \times 14$ k-point grid was used for PDOS analysis. High-symmetry k-points were selected for band structure calculations.

Geometry optimization and energy convergence were performed using the Broyden–Fletcher–Goldfarb–Shanno (BFGS) algorithm,[79] with a stringent convergence threshold of 1×10^{-8} eV. Hubbard U corrections were applied systematically to all Zn and Ag with $U(Zn) = 10$ eV and $U(Ag) = 6$ eV, respectively, to properly justify the correlated d and p electrons. The Ag/ZnO/GO hybrid system is larger, asymmetric, and more complex. GO was represented by an ideal planar hydrogen-passivated flake with standard deviation of the z-coordinates z-SD ≈ 0.12 Å in a 30 Å $\times$ 30 Å $\times$ 40 Å box. The hydrogen-terminated Ag/Zn_7O_8

Table 3 Comparison of the photocatalytic dye removal efficiency of this work with existing literature

| Photocatalyst	Dye type	Photocatalytic efficiency (%)	Irradiation time (min)	Catalyst loading (mg)	Light source	Dye concentration (ppm)	Rate constant ($\times 10^{-2}$ min^{-1})	Ref.
ZnO	Methylene Blue	98		100	Philips TL 8W	5	~0.089	70
(Ag and Ni)–ZnO	Methyl Orange	99.93	160	100	UV light, 8 W	10	—	71
Ag doped ZnO	Methylene Blue	~98	30	100	Intensity 1 sun	10	~13	72
	Rose Bengal (RB)	~96					~10	
(Cu and Ni)–ZnO	Methyl Orange	94.4	180	210	Four UV lights (80 W)	10	~1.17	73
(Sb and W) ZnO	Methylene Blue	~91	120	300	6W UV A lamp	10	—	74
ZnO/GO	Methylene Blue	~91	80	1000	Visible light 500 W	96	—	75
Ag/GO/ZnO	Methylene Blue	97.53	180	300	100 W UV light	15	~5.198	36
Fe–ZnO/GO	Rhodamine B	99.32	1440	50	Natural sunlight	10	~0.3488	34
(Ag and Cu)–GO/ZnO	Brilliant Yellow	100	90	—	Sunlight	10	~1.112	1
Ag/ZnO/GO	Methylene Blue	99.9	80	65	UV lamp	15	~5.57	This work
	Methyl Red	92				30	~2.50	
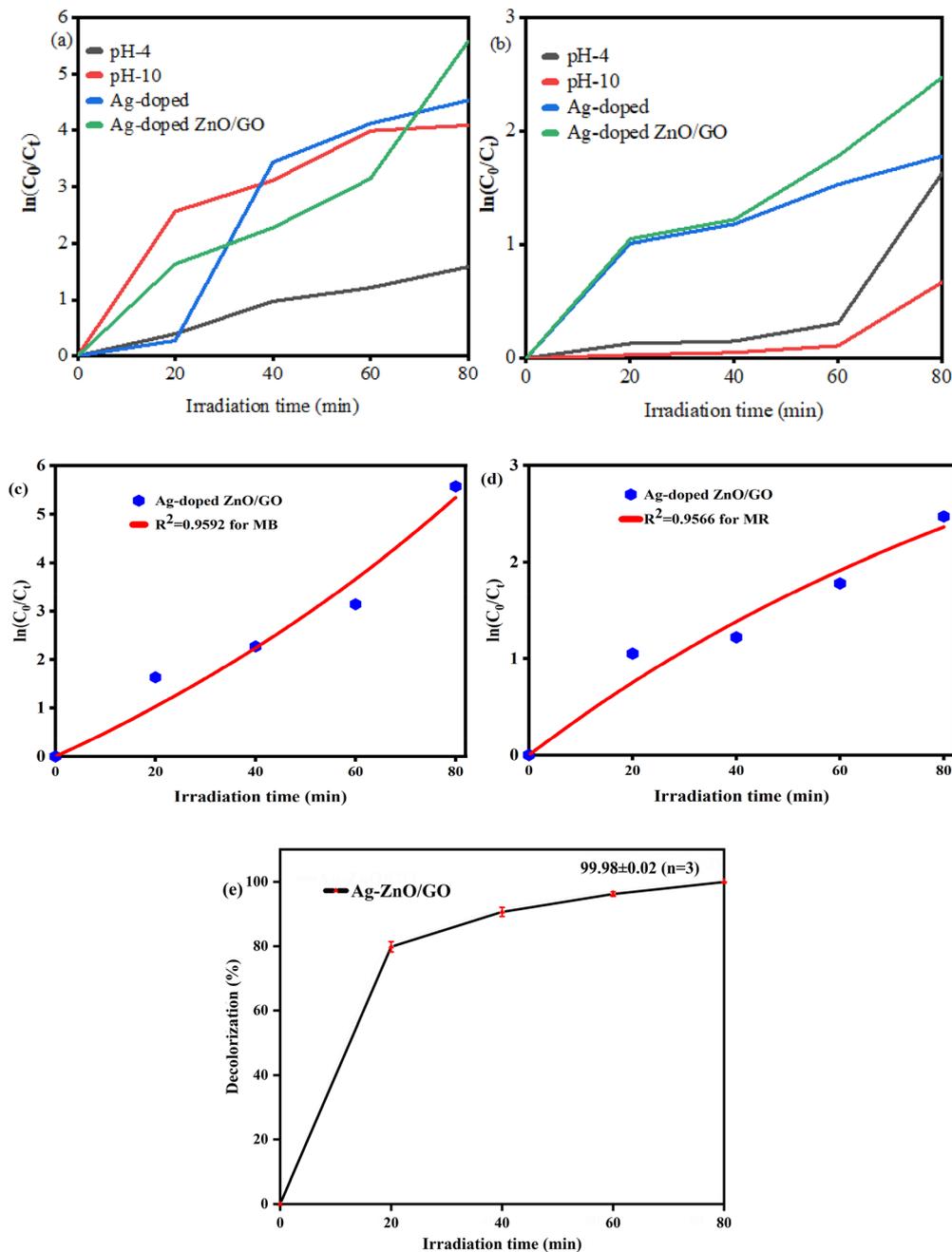
Fig. 10 Pseudo-first-order kinetics of (a) MB and (b) MR adsorption on undoped ZnO, Ag-doped ZnO, and Ag-doped ZnO/GO; R^2 for photocatalytic activity of Ag-doped ZnO/GO (c) toward MB and (d) toward MR, and (e) triplicate measurement error bar.

cluster was placed ≈ 3.0 Å above GO to construct the Zn_8O_8/GO heterostructure, and fully optimized MB and MR dyes were placed ≈ 3 Å above the Zn_8O_8 surface to create MB/MR–Zn_8O_8–GO assemblies. The atoms' relaxation was carried out until the magnitude of the force was below 0.001 Ry Bohr^{-1}, and adsorption energy was calculated.

The results for electronic band structures and partial density of states (PDOS) are shown in Fig. 11(a–f). For pure ZnO (Fig. 11a and d), a direct bandgap of 3.26 eV at the Γ point was observed.[23] In the valence band region, the O-2p states are

dominant.[80] In the conduction band region, the main contributors are the Zn-4s and Zn-4p states, with contributions comparable to those from the O states. This confirms the semiconducting properties of ZnO.[81,82] The presence of Ag-4d states exhibits weak contributions across the electronic states. A further decrease in the bandgap of the Ag:ZnO/GO nanocomposite (Fig. 11c) to 2.46 eV was observed and PDOS (Fig. 11(f)) shows the contributions from Ag, C, O, and Zn orbitals, showing that electrons move efficiently between ZnO, Ag, and GO. Following O-2p states, a prominent contribution is observed
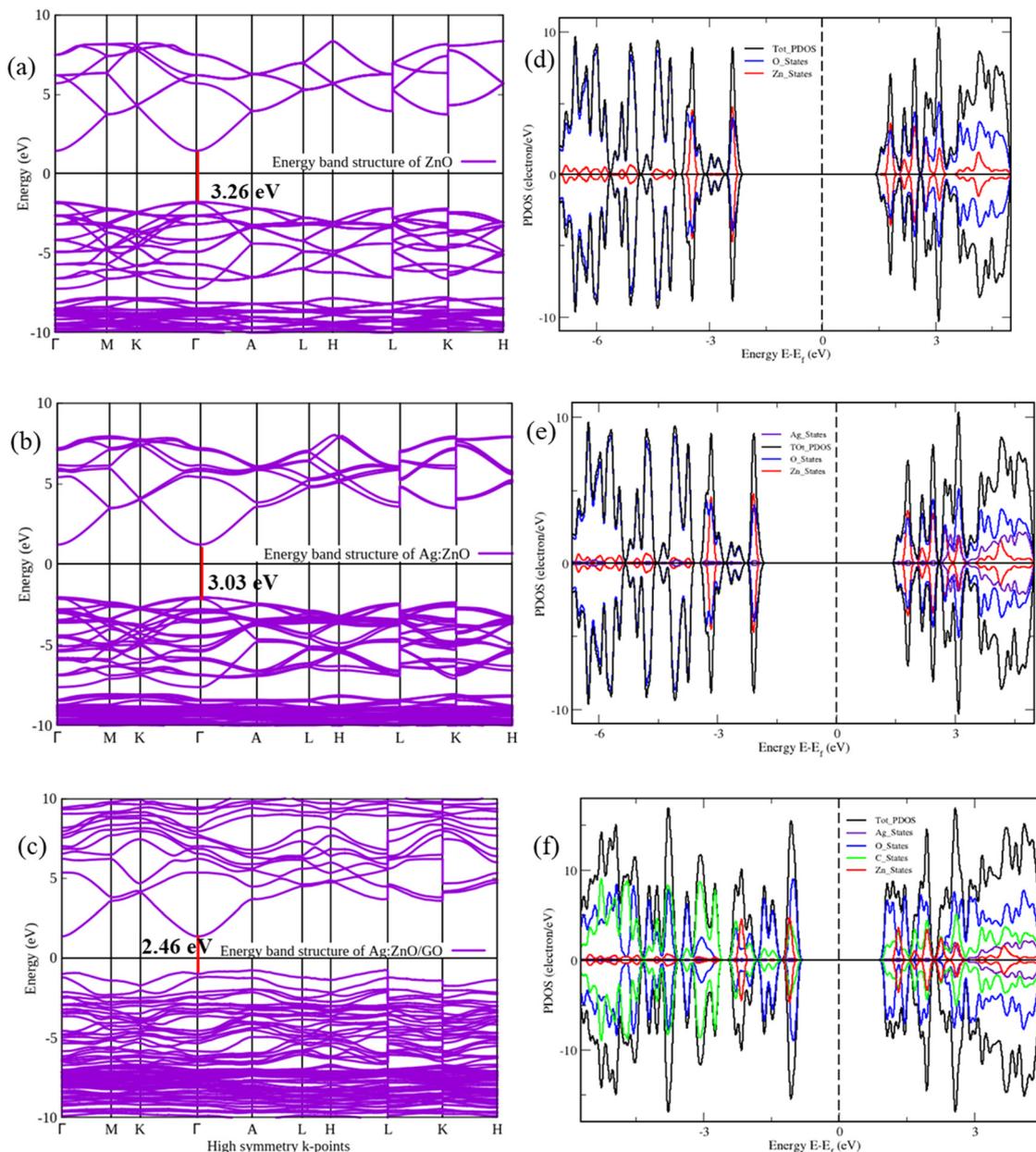
Fig. 11   Band structure and PDOS (spin up and down) (a) and (d) for pure-ZnO, (b) and (e) for Ag-doped ZnO, and (c) and (f) for Ag-doped ZnO/GO NPs.

from the C-2p states, which indicates obvious O–C hybridization.

Consequently, Ag:ZnO/GO exhibited better performance than pure ZnO and Ag-doped ZnO due to the synergetic effect of Ag doping and GO addition, extending its light absorption in the visible range and improving charge separation. From the theoretical analysis, the Ag and graphene oxide-induced modulation of the ZnO electronic structure, with the associated increase in the density of states at the Fermi level, provides a basis for the experimentally observed enhancement of the photocatalytic activity.

The difference between the experimental band gaps of 3.00 eV for Ag–ZnO/GO obtained from UV-Vis DRS and a lower

theoretical band gap, 2.46 eV, calculated by DFT+U, could be attributed for the intrinsic limitations of the computational model. The supercell model used in DFT represents an idealized Ag–ZnO/GO interface with fixed defect density and nanoscale geometry, whereas the actual experimental nanocomposite

Table 4   Calculated adsorption energy of MB/MR onto undoped and Ag-doped ZnO/GO

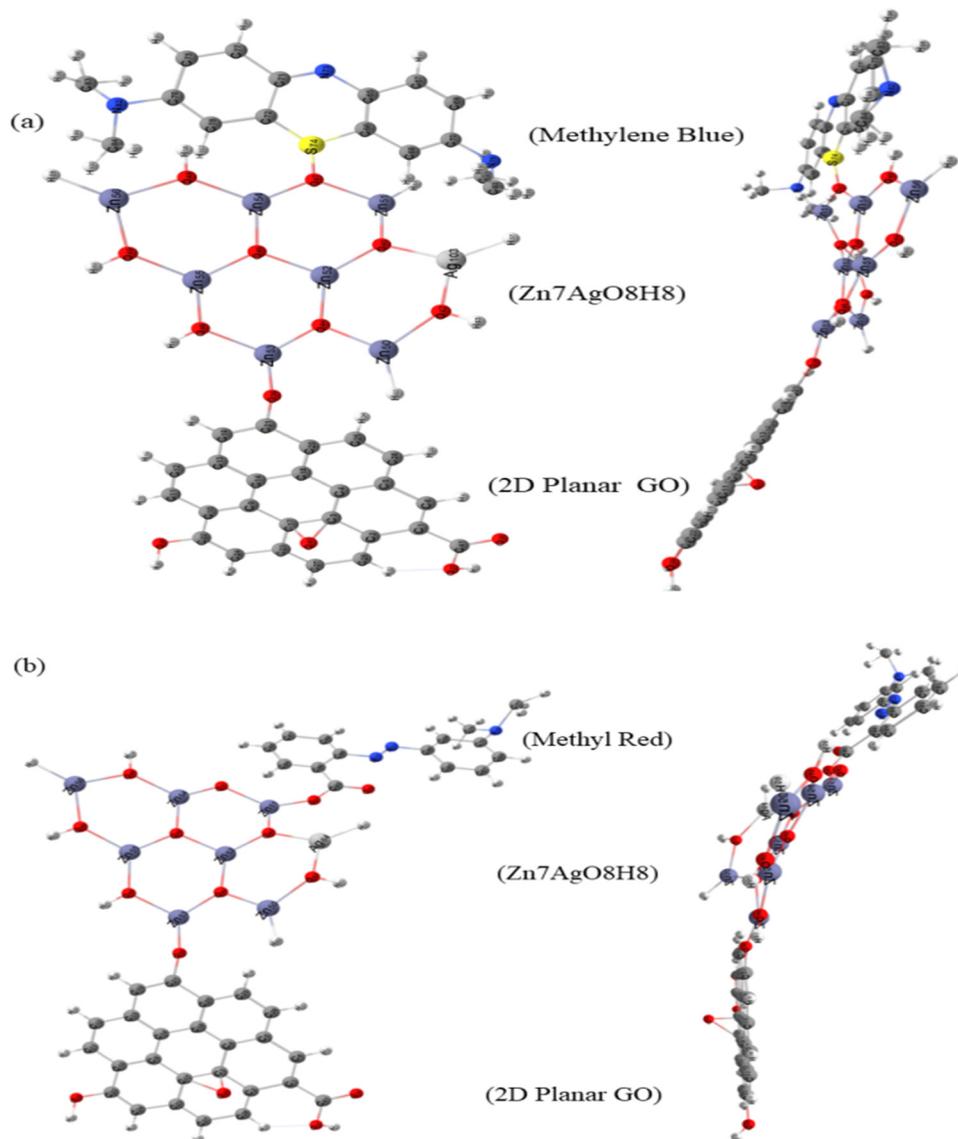| Systems	MB/ ZnO	MB/Ag/ ZnO	MB/Ag/ ZnO/GO	MR/ ZnO	MR/Ag/ ZnO	MR/Ag/ ZnO/GO
E_{ads} (eV)	−0.809	−1.150	−1.490	−0.337	−0.986	−1.611

Fig. 12 Optimized adsorption structure of Ag-doped ZnO with 2D planar GO for (a) Methylene Blue and (b) Methyl Red.

Table 5 Net Mulliken charges for the isolated fragments and complex system

Complex system	Complex Q (e)	Donor (isolated)	Donor Q (e)	Dye (isolated)	Dye Q (e)	$\sum$Isolated (e)	ΔQ (e)
ZnO + MB	1.1940	ZnO	0.6952	MB	0.5708	1.266	−0.0720
ZnO + Ag + MB	1.1496	Ag:ZnO	0.6540	MB	0.5708	1.2248	−0.0752
ZnO + Ag + GO + MB	1.5329	Ag:ZnO/GO	1.1194	MB	0.5708	1.6902	−0.1573
ZnO + MR	1.1030	ZnO	0.6952	MR	0.4965	1.1917	−0.0887
ZnO + Ag + MR	0.9880	Ag:ZnO	0.6540	MR	0.4965	1.1505	−0.1625
ZnO + Ag + GO + MR	1.4454	Ag:ZnO/GO	1.1194	MR	0.4965	1.6159	−0.1705

contains larger particle sizes, surface states, interfacial defects, and quantum-confinement variations. These structural and morphological factors contribute to a wider experimental optical band gap compared to the DFT-predicted value. Thus, the 0.54 eV variance falls within the expected theoretical–experimental deviations, and the overall trend of band gap narrowing upon Ag and GO incorporation is fully consistent across both approaches.

3.7. Adsorption of dyes

Adsorption energy (E_{ads}) is one tool used for describing the strength of attachment of dye molecules onto a photocatalyst's
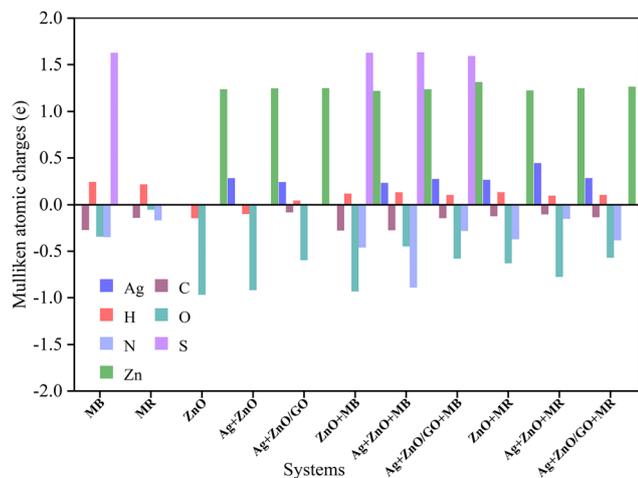
Fig. 13 Mulliken charge population analysis of isolated and adsorbed systems.

surface.[83] A more negative value of E_{ads} will indicate stronger interaction, which commonly improves the performance of the photocatalyst by enhancing the transfer of charges between the dye and catalyst.[23,83] In this study, we examined how Methylene Blue (MB) and Methylene Red (MR) dyes interact with pure ZnO, Ag-doped ZnO, and Ag/ZnO/GO composite surfaces to see how these modifications affect adsorption strength and photocatalytic efficiency. For Methylene Blue dye, the E_{ads} values were -0.809 eV for MB/ZnO, -1.150 eV for MB/Ag/ZnO, and -1.490 eV for MB/Ag/ZnO/GO (see Table 4). It can be noted that with increasing E_{ads} absolute value, both silver and GO contribute to the enhancement of the MB–catalyst interaction. The highest E_{ads} value is observed in MB/Ag/ZnO/GO with -1.490 eV. This indicates that the combined influence of silver and GO is able to provide a reactive interface to allow firm binding and efficient electron transfer. This will allow it to degrade MB effectively with illumination.[84]

A similar trend was observed with Methylene Red. The adsorption energies for MR/ZnO, MR/Ag/ZnO, and MR/Ag/ZnO/GO were -0.337 eV, -0.986 eV, and -1.611 eV, respectively (see Table 4). Once again, the Ag/ZnO/GO composite exhibited the strongest adsorption, indicating that it offers more active sites and facilitates improved separation of photoinduced electrons and holes, both of which are essential components of effective photocatalysis. The highest adsorption energy values for the Ag/ZnO/GO composite were -1.490 eV for MB and -1.611 eV for MR. These highly negative values are significant since they confirm that the strongest and most energetically favorable interaction between the dyes and the optimized composite surface takes place. This validates the experimental observation of high photocatalytic dye removal efficiency (Fig. 12).

Overall, the findings clearly demonstrate that the adsorption of both dyes is greatly enhanced when Ag and GO are added to ZnO. All systems had negative E_{ads} values, confirming that dye adsorption is spontaneous and energetically favorable.[84] Among all, the Ag/ZnO/GO composite demonstrated the most

stable and effective dye adsorption, which aligns well with experimental observations showing higher decolorization efficiency for this system.

3.8. Mulliken charge distribution analysis

Charge redistribution at the dye–semiconductor interface was analyzed using Mulliken population analysis, providing a qualitative estimate due to its basis-set dependence. The charge transfer (ΔQ) was calculated as:[83]

$$\Delta Q = Q_{Complex} - (Q_{Dye} + Q_{Substrate}) \qquad (6)$$

In Table 5, the results clearly reveal a stepwise improvement of electron transfer in the order ZnO, Ag:ZnO and Ag:ZnO/GO, demonstrating that the synergistic interaction between Ag and GO improves the mobility of charges.[83,85]

As evident from the results presented in Table 5, there is an increase in magnitude of each ΔQ value corresponding to MB and MR from ZnO to Ag–ZnO to Ag–ZnO/GO. The increased charge transfer signifies that the MB molecule receives substantial electron density from the semiconductor surface, hence proving to be an electron acceptor.[85,86] The large ΔQ value also reveals strong interfacial coupling between the MB π-system and the conduction-band states of Ag–ZnO/GO, ensuring efficient charge delocalization and suppression of recombination losses.[87] By contrast, MR shows relatively smaller overall charge redistribution increases from ZnO to Ag–ZnO and further to Ag–ZnO/GO (Fig. 13).[83,85,86]

Although MR also acts as an electron acceptor,[85] its ΔQ increase is smaller than that of MB, suggesting a weaker interaction with the surface. This difference is mainly related to their molecular structures: MB has a more extended π-conjugated system that helps it capture electrons more easily,[88] whereas MR is less conjugated and therefore traps electrons less effectively.[89] The increase in ΔQ after adding Ag and GO indicates that both components assist charge transfer at the interface,[86] giving the Ag–ZnO/GO composite the most favorable charge distribution. As a result, the ternary Ag–ZnO/GO composite possesses the most favorable charge distribution, corresponding to the largest ΔQ and highest predicted photocatalytic efficiency.

A schematic photocatalytic dye removal pathway is proposed in Fig. 14(a), for Methylene Blue[90] and (b) for Methyl Red,[91] based on what has been observed in the experiments, the scavenger results, and the DFT analysis. It primarily illustrates the role of the semiconductor material ZnO as the photoactive component, Ag as the electron mediator, and the use of conductive GO as the supporting material for interfacial charge transfer. The presence of Ag nanoparticles and graphene oxide (GO) facilitates charge separation. Ag acts as an electron sink, while GO serves as a conductive electron transport pathway, suppressing electron–hole recombination. This is clearly proposed as a hypothetical scheme, based on the results that have been observed.[90,91]

A negative ΔQ means net electron accumulation on the complex relative to the isolated fragments. Fragment-resolved changes presented in Table 4 tell us that ZnO becomes slightly
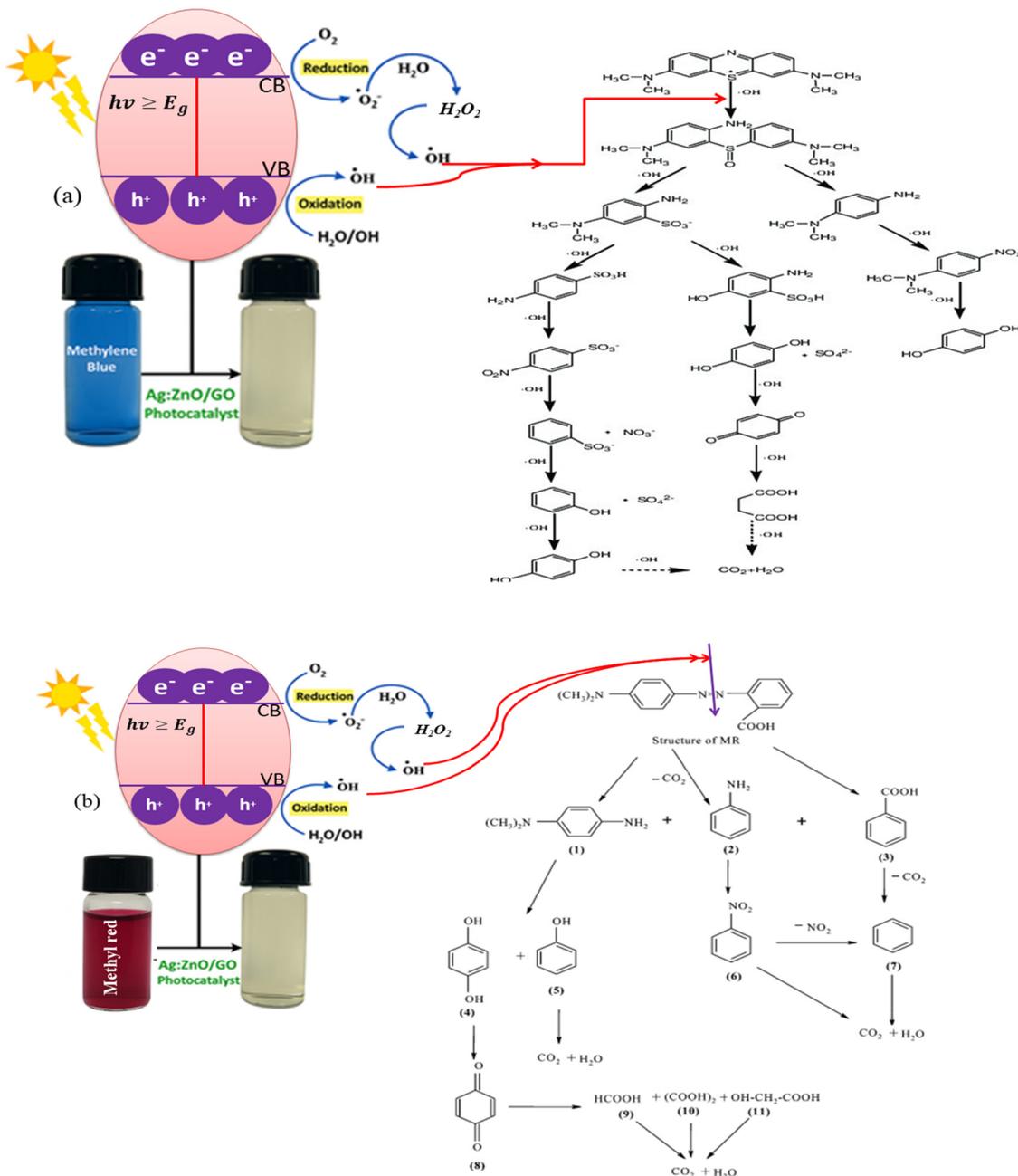
Fig. 14 Illustrative decolorization mechanism and paths for (a) Methylene Blue dye and (b) Methyl Red dye.

more positive, while the dye becomes less positive, which points to electron redistribution from ZnO to the dye. Overall, the Mulliken charge-transfer analysis provides evidence that both MB and MR behave as electron acceptors, with MB displaying better interfacial electron affinity and coupling to the semiconductor. These results are in excellent agreement with the experimentally observed higher rates of photocatalytic dye removal of MB as compared with MR under identical photocatalytic conditions.[85] Mineralization analysis, such as total organic carbon (TOC) measurements, would be required to fully quantify organic carbon conversion. In this study, the strong photocatalytic activity of the Ag–ZnO/GO composite is supported by experimental and theoretical evidence, including reduced electron–hole recombination (PL analysis), band gap narrowing (UV-Vis DRS), and strong adsorption interactions predicted by DFT calculations. These results indicate that the Ag–ZnO/GO nanocomposite enhances efficient photocatalytic oxidation of dye molecules under visible light.

4. Conclusions

Undoped ZnO, Ag-doped ZnO, and Ag-doped ZnO/GO nanocomposites were successfully synthesized by the co-precipitation method. The Ag-doped ZnO/GO nanocomposites

exhibited superior photocatalytic activity as confirmed both experimentally and computationally. Structural, optical, and computational analysis illustrated the evident effect of Ag and GO on ZnO morphology, crystal properties, bandgap, absorption abilities, and electron mobility. The photocatalytic efficiency experiment shows the highest MB decolorization of 99.98 ± 0.02 ($n = 3$)% and strong decoloration of Methyl Red of 92% in only 80 minutes. The outstanding recyclability and stability even after five cycles for removal of MB, caused by the combined effect of the Ag nanoparticles on the ZnO/GO nanocomposites, occurs due to the formation of Schottky barriers that effectively trap electrons, with the help of fast conductive channels provided by GO for the efficient transfer of electrons, hence effectively preventing recombination processes. The density functional theory and Mulliken computations also supported the efficient rearrangement of charges with strong interactions with the MB molecule upon interactions of the Ag/ZnO/GO nanocomposites, hence validating the proposed mechanism with superior practical efficiency. The synergistic interaction between Ag nanoparticles and GO sheets enhances visible-light absorption, promotes efficient charge separation, and facilitates the generation of reactive oxygen species responsible for dye degradation. This work provides an in-depth insight into the structure property activity relationship in the Ag/ZnO/GO nanocomposites, hence showcasing their huge potential application in the efficient decomposition of environmental pollutants with minimum cost due to the high recyclability with outstanding activity efficiency as a photocatalyst.

Conflicts of interest

There are no conflicts to declare.

Data availability

The data not included in the manuscript are available from the corresponding author upon request.

Acknowledgements

References

1 N. A. Al-Rawashdeh, O. Allabadi and M. T. Aljarrah, Photocatalytic activity of graphene oxide/zinc oxide nanocomposites with embedded metal nanoparticles for the degradation of organic dyes, *ACS Omega*, 2020, **5**(43), 28046–28055.

2 P. Zhang, *et al.*, Vertically aligned graphene sheets membrane for highly efficient solar thermal generation of clean water, *ACS Nano*, 2017, **11**(5), 5087–5093.

3 J. Romao, *et al.*, High throughput analysis of photocatalytic water purification, *Anal. Chem.*, 2014, **86**(15), 7612–7617.

4 Y. Shen, *et al.*, Constructing three-dimensional hierarchical architectures by integrating carbon nanofibers into graphite felts for water purification, *ACS Sustainable Chem. Eng.*, 2016, **4**(4), 2351–2358.

5 X. Fang, *et al.*, Inorganic semiconductor nanostructures and their field-emission applications, *J. Mater. Chem.*, 2008, **18**(5), 509–522.

6 L. Xu, W. Chu and L. Gan, Environmental application of graphene-based CoFe$_2$O$_4$ as an activator of peroxymonosulfate for the degradation of a plasticizer, *Chem. Eng. J.*, 2015, **263**, 435–443.

7 G. WH, Description of a kinetic model for the oxidation of hazardous materials in aqueous media with ozone and hydrogen peroxide in a semi-batch reactor, *Ind. Eng. Chem. Res.*, 1989, **28**, 1573–1580.

8 V. Kumari, S. Kaushal and P. P. Singh, Green synthesis of a CuO/rGO nanocomposite using a *Terminalia arjuna* bark extract and its catalytic activity for the purification of water, *Mater. Adv.*, 2022, **3**(4), 2170–2184.

9 K. Bano, *et al.*, Sunlight driven photocatalytic degradation of organic pollutants using a MnV$_2$O$_6$/BiVO$_4$ heterojunction: Mechanistic perception and degradation pathways, *Nanoscale Adv.*, 2021, **3**(22), 6446–6458.

10 P. P. Singh, *et al.*, Construction of a 3D flower-like NiO/Mn$_3$O$_4$ heterojunction using Tulsi leaf extract for enhanced photodegradation of thiamethoxam pesticide and organic dyes under direct sunlight, *Mater. Adv.*, 2024, **5**(20), 8097–8110.

11 K. Bano, *et al.*, Construction of honey bee hive-like CuO/PbO heterojunction photocatalysts with enhanced antibiotic and dye degradation activity under visible light, *Environ. Sci.: Water Res. Technol.*, 2024, **10**(7), 1714–1725.

12 M. Mahajan, *et al.*, Role of cellulose, phenolic compounds, and water-soluble proteins in ZnO nanoparticle synthesis using Mangifera indica leaf extract for photocatalytic and antioxidant investigations, *Colloids Surf., A*, 2025, **720**, 137066.

13 K. Katyal, *et al.*, Phyto-engineered zinc oxide nanoparticles with tunable morphology for sustainable environmental and biomedical applications, *Inorg. Chem. Commun.*, 2025, **179**, 114859.

14 K. Bano, *et al.*, Fabrication of CuO/ZnO heterojunction photocatalyst for efficient photocatalytic degradation of tetracycline and ciprofloxacin under direct sun light, *Environ. Nanotechnol., Monit. Manage.*, 2023, **20**, 100863.

15 K. Virk, *et al.*, Functionalized gum acacia hydrogels with silver nanoparticles for enhanced antimicrobial and environmental applications, *Appl. Organomet. Chem.*, 2025, **39**(8), e70309.

16 B. Kaur, *et al.*, Facile synthesis of CTAB-Co$_3$O$_4$ quantum dots for pollutant dye remediation: UV light triggered photocatalyst, *ChemistrySelect*, 2025, **10**(35), e02613.

17 M. Dagar, *et al.*, Synergistic Ce/Ag/N-doped ZnO-MWCNT nanocomposites for efficient photocatalytic wastewater remediation with visible light, *Mater. Adv.*, 2025, **6**(13), 4522–4537.

18 A. K. Shimi, *et al.*, Green synthesis of SrO nanoparticles using leaf extract of *Albizia julibrissin* and its recyclable photocatalytic activity: an eco-friendly approach for treatment of industrial wastewater, *Environ. Sci.: Adv.*, 2022, **1**(5), 849–861.

19 S. Rohilla, *et al.*, Excellent UV-light triggered photocatalytic performance of ZnO. SiO$_2$ nanocomposite for water pollutant compound methyl orange dye, *Nanomaterials*, 2021, **11**(10), 2548.

20 R. Kumar, *et al.*, Efficient ZnO-based visible-light-driven photocatalyst for antibacterial applications, *ACS Appl. Mater. Interfaces*, 2014, **6**(15), 13138–13148.

21 S. J. Armaković, *et al.*, ZnO-based photocatalysts: synergistic effects of material modifications and machine learning optimization, *Catalysts*, 2025, **15**(8), 793.

22 E. Matei, *et al.*, ZnO nanostructured matrix as nexus catalysts for the removal of emerging pollutants, *Environ. Sci. Pollut. Res.*, 2023, **30**(54), 114779–114821.

23 K. Belachew, *et al.*, Tailoring photocatalytic degradation properties of ZnO nanoparticles via metal doping: insights from synthesis, characterization, and DFT calculations, *J. Mater. Sci.: Mater. Electron.*, 2025, **36**(16), 929.

24 I. Aadnan, *et al.*, Structural, optical and photocatalytic properties of Mn Doped ZnO nanoparticles used as photocatalysts for Azo-dye degradation under visible light, *Catalysts*, 2022, **12**(11), 1382.

25 A. Muhammed, T. G. Asere and T. F. Diriba, Photocatalytic and antimicrobial properties of ZnO and Mg-doped ZnO nanoparticles synthesized using Lupinus albus leaf extract, *ACS Omega*, 2024, **9**(2), 2480–2490.

26 H. D. Kiriarachchi, *et al.*, Growth mechanism of sea urchin ZnO nanostructures in aqueous solutions and their photocatalytic activity for the degradation of organic dyes, *ACS Omega*, 2019, **4**(9), 14013–14020.

27 A. Pujara, *et al.*, Novel zinc oxide 3D tetrapod nano-microstructures: recent progress in synthesis, modification and tailoring of optical properties for photocatalytic applications, *Mater. Adv.*, 2025, **6**(7), 2123–2153.

28 K. Mohamed, *et al.*, Recent advances in ZnO-based nanostructures for the photocatalytic degradation of hazardous, non-biodegradable medicines, *Crystals*, 2023, **13**(2), 329.

29 A. Ojha, T. A. Samriti and J. Prakash, Graphene family nanomaterials as emerging sole layered nanomaterials for wastewater treatment: recent developments, potential hazards, prevention and future prospects, *Environ. Adv.*, 2023, **13**, 100402.

30 P. Majumder and R. Gangopadhyay, Evolution of graphene oxide (GO)-based nanohybrid materials with diverse compositions: an overview, *RSC Adv.*, 2022, **12**(9), 5686–5719.

31 L. Y. Ozer, *et al.*, Inorganic semiconductors-graphene composites in photo (electro) catalysis: synthetic strategies, interaction mechanisms and applications, *J. Photochem. Photobiol., C*, 2017, **33**, 132–164.

32 L. Dai, *et al.*, Metal-free catalysts for oxygen reduction reaction, *Chem. Rev.*, 2015, **115**(11), 4823–4892.

33 H. A. Chauhan, *et al.*, Photocatalytic activity of graphene oxide/zinc oxide nanocomposite derived from rice husk for the degradation of phenanthrene under ultraviolet-visible light, *J. Water Process Eng.*, 2022, **47**, 102714.

34 T. Imboon, *et al.*, Synergistic effects of Fe-doped ZnO and graphene oxide for enhanced photocatalytic performance and tunable magnetic properties, *ACS Omega*, 2025, **10**(31), 34571–34587.

35 J. Qin, *et al.*, Ag/ZnO/graphene oxide heterostructure for the removal of rhodamine B by the synergistic adsorption–degradation effects, *Ceram. Int.*, 2015, **41**(3), 4231–4237.

36 M. R. Al-Mamun, *et al.*, A novel and highly efficient Ag and GO co-synthesized ZnO nano photocatalyst for methylene blue dye degradation under UV irradiation, *Environ. Nanotechnol., Monit. Manag.*, 2021, **16**, 100495.

37 X. Yan, *et al.*, Is methylene blue an appropriate substrate for a photocatalytic activity test? A study with visible-light responsive titania, *Chem. Phys. Lett.*, 2006, **429**(4–6), 606–610.

38 T. G. Jaik, *et al.*, Correction: Thermal response and thermochromism of methyl red-based copolymer systems-coupled responsiveness in critical solution behaviour and optical absorption properties, *Polym. Chem.*, 2022, **13**(9), 1282.

39 S. N. Yadav, *et al.*, Interaction between methyl red and cetyltrimethylammonium bromide under the influence of sodium polystyrene sulphonate in ethanol-water binary solvent systems: a spectrophotometric investigation, *Heliyon*, 2024, **10**(12), e33014.

40 E. Goh, J. Mah and T. Yoon, Effects of Hubbard term correction on the structural parameters and electronic properties of wurtzite ZnO, *Comput. Mater. Sci.*, 2017, **138**, 111–116.

41 E. M. Flores, M. R. L. Moreira and M. J. Piotrowski, Structural and electronic properties of bulk ZnX (X= O, S, Se, Te), ZnF$_2$, and ZnO/ZnF$_2$: a DFT investigation within PBE, PBE+*U*, and hybrid HSE functionals, *J. Phys. Chem. A*, 2020, **124**(19), 3778–3785.

42 N. Hamzah, *et al.*, A DFT+*U* study of structural, electronic and optical properties of Ag-and Cu-doped ZnO, *Microelectron. Int.*, 2023, **40**(1), 53–62.

43 Heryanto, *et al.*, Quantitative analysis of X-ray diffraction spectra for determine structural properties and deformation energy of Al, Cu and Si, *J. Phys.: Conf. Ser.*, 2019, **1317**, 012052.

44 M. Pozzi, *et al.*, Visualization of the high surface-to-volume ratio of nanomaterials and its consequences, *J. Chem. Educ.*, 2024, **101**(8), 3146–3155.

45 K. Ravichandran, *et al.*, Fabrication of ZnO:Ag/GO composite thin films for enhanced photocatalytic activity, *Ceram. Int.*, 2017, **43**(13), 10041–10051.

46 H. Sadiq, *et al.*, Preparation and photocatalytic degradation of ZnO/Fe$_3$O$_4$/GO heterojunction *via* synergistic electron–hole separation, *Mater. Sci. Eng., B*, 2026, **324**, 118903.

47 K. Shaik and S. Cole, Comparative study of crystallite size from XRD and TEM results for pure and V$_2$O$_5$ doped CdO-FePO$_4$ composite nanopowders, *Phys. Chem. Res.*, 2023, **11**(2), 241–251.

48 A. Hussain, *et al.*, Optimizing photocatalytic performance with Ag-doped ZnO nanoparticles: Synthesis and characterization, *Heliyon*, 2024, **10**(15), e35725.

49 Y. Guan, *et al.*, Green one-step synthesis of ZnO/cellulose nanocrystal hybrids with modulated morphologies and superfast absorption of cationic dyes, *Int. J. Biol. Macromol.*, 2019, **132**, 51–62.

50 A. R. Kachere, *et al.*, Zinc oxide/graphene oxide nanocomposites: synthesis, characterization and their optical properties, *ES Mater. Manuf.*, 2021, **16**(6), 19–29.

51 S. S. Patil, *et al.*, Green approach for hierarchical nanostructured Ag-ZnO and their photocatalytic performance under sunlight, *Catal. Today*, 2016, **260**, 126–134.

52 U. Ali, *et al.*, Graphene oxide incorporation in Ag-doped ZnO nanocomposite as efficient electron extraction material for planar perovskite solar cells, *Results in Optics*, 2023, **12**, 2023.

53 H. Afzal, *et al.*, Enhanced drug efficiency of doped ZnO–GO (graphene oxide) nanocomposites, a new gateway in drug delivery systems (DDSs), *Mater. Res. Express*, 2020, **7**(1), 015405.

54 P. Sun, Z. Lv and C. Sun, Study on the synthesis of nano zinc oxide particles under supercritical hydrothermal conditions, *Nanomaterials*, 2024, **14**(10), 844.

55 O. Muktaridha, *et al.*, Progress of 3d metal-doped zinc oxide nanoparticles and the photocatalytic properties, *Arabian J. Chem.*, 2021, **14**(6), 103175.

56 O. R. Vasile, *et al.*, Influence of the size and the morphology of ZnO nanoparticles on cell viability, *C. R. Chim*, 2015, **18**(12), 1335–1343.

57 A. S. Ajayan and N. Hebsur, Green synthesis of zinc oxide nanoparticles using neem (*Azadirachta indica*) and Tulasi (*Ocimum tenuiflorum*) leaf extract and their characterisation, *Int. J. Curr. Microbiol. Appl. Sci.*, 2020, **9**(2), 277–285.

58 A. Anžlovar, Z. Crnjak Orel and M. Žigon, Nanocomposites with nano-to-sub-micrometer size zinc oxide as an effective UV absorber, *Polimeri*, 2008, **29**(2), 84–87.

59 P. A. Luque-Morales, *et al.*, ZnO semiconductor nanoparticles and their application in photocatalytic degradation of various organic dyes, *Materials*, 2021, **14**(24), 7537.

60 S. Sagadevan, *et al.*, Structural, dielectric and optical investigation of chemically synthesized Ag-doped ZnO nanoparticles composites, *J. Sol–Gel Sci. Technol.*, 2017, **83**(2), 394–404.

61 V. H. Tran Thi, *et al.*, Synergistic adsorption and photocatalytic activity under visible irradiation using Ag-ZnO/GO nanoparticles derived at low temperature, *J. Chem.*, 2019, **2019**(1), 2979517.

62 S. P. Yeap, Permanent agglomerates in powdered nanoparticles: formation and future prospects, *Powder Technol.*, 2018, **323**, 51–59.

63 A. Kocjan, M. Logar and Z. Shen, The agglomeration, coalescence and sliding of nanoparticles, leading to the rapid sintering of zirconia nanoceramics, *Sci. Rep.*, 2017, **7**, 2541.

64 X. Wang, *et al.*, Roles of pH, cation valence, and ionic strength in the stability and aggregation behavior of zinc oxide nanoparticles, *J. Environ. Manage.*, 2020, **267**, 110656.

65 J. Wu, *et al.*, Preparation and characterization of GO/ZnO/Ag nanocomposites and their synergistic antibacterial effect on *Streptococcus mutans*, *AIP Adv.*, 2023, **13**(3), 035313.

66 S. Gea, *et al.*, Facile synthesis of ZnO-Ag nanocomposite supported by graphene oxide with stabilised band-gap and wider visible-light region for photocatalyst application, *J. Mater. Res. Technol.*, 2022, **19**, 2730–2741.

67 I. Daou, O. Zegaoui and A. Elghazouani, Physicochemical and photocatalytic properties of the ZnO particles synthesized by two different methods using three different precursors, *C. R. Chim*, 2017, **20**(1), 47–54.

68 H. Tran, *et al.*, Kinetics of photocatalytic degradation of organic compounds: a mini-review and new approach, *RSC Adv.*, 2023, **13**, 16915–16925.

69 A. N. Abdulqodus, *et al.*, Green synthesis of ZnO nanoparticles: effect of pH on morphology and photocatalytic degradation efficiency, *Appl. Phys. A*, 2025, **131**(9), 720.

70 M. T. Masuleh, M. Hasheminiasari and R. Ashiri, Enhanced photocatalytic efficiency of eco-friendly synthesized ZnO for rapid full degradation of methylene blue dye, *Mater. Adv.*, 2025, **6**(8), 2611–2621.

71 A. Azfar, *et al.*, Comparative study on photocatalytic activity of transition metals (Ag and Ni)-doped ZnO nanomaterials synthesized via sol–gel method, *R. Soc. Open Sci.*, 2020, **7**(2), 191590.

72 S. S. Wagh, *et al.*, Comparative studies on synthesis, characterization and photocatalytic activity of Ag doped ZnO nanoparticles, *ACS Omega*, 2023, **8**(8), 7779–7790.

73 M. R. Al-Mamun, *et al.*, Enhanced photocatalytic activity of Cu and Ni-doped ZnO nanostructures: a comparative study of methyl orange dye degradation in aqueous solution, *Heliyon*, 2023, **9**(6), e16506.

74 S. Modi, *et al.*, Photocatalytic degradation of methylene blue dye from wastewater by using doped zinc oxide nanoparticles, *Water*, 2023, **15**(12), 2275.

75 S. Al-Zahrani, *et al.*, Biomass mediated synthesis of ZnO and ZnO/GO for the decolorization of Methylene Blue under visible light source, *Catalysts*, 2023, **13**, 409, DOI: 10.3390/catal13020409.

76 J. N. Ding, X. Q. Wang and N. Y. Yuan, DFT study of structure, electronic, optical and magnetic properties of ZnO and Cu-doped ZnO clusters, *Key Eng. Mater.*, 2011, **483**, 569–573.

77 S. Ramesh, *et al.*, Nanorod-like structure of ZnO nanoparticles and Zn_8O_8 clusters using 4-dimethylamino benzaldehyde liquid to study the physicochemical and antimicrobial properties of pathogenic bacteria, *Nanomaterials*, 2022, **13**(1), 166.

78 H.-K. Tian, *et al.*, Identification of double-Chain Zn_8O_8 structure on ZrO_2 as a highly active site for CO_2 hydrogenation to methanol, *J. Phys. Chem. Lett.*, 2025, **16**(36), 9444–9452.

79 J. D. Head and M. C. Zerner, A Broyden---Fletcher---Goldfarb—Shanno optimization procedure for molecular geometries, *Chem. Phys. Lett.*, 1985, **122**(3), 264–270.

80 I. M. Kahura, S. Kiprotich and W. M. Mulwa, Energy band-gap engineering for ZnO as a photoanode of dye sensitized

solar cells; an *ab initio* study, *Am. J. Mater. Sci.*, 2024, **14**(2), 31–44.

81 S. U. Awan, *et al.*, Defects mediated weak ferromagnetism in $Zn_{1-y}C_yO$ $(0.00 \leq y \leq 0.10)$ nanorods semiconductors for spintronics applications, *Sci. Rep.*, 2023, **13**(1), 17080.

82 I. M. Kahura, K. Sharon and W. M. Mulwa, Energy band-gap engineering for ZnO as a photoanode of dye sensitized solar cells; an *ab initio* study, *Am. J. Mater. Sci.*, 2024, **14**(2), 31–44.

83 L. Zhou, H. Zhu and W. Zeng, Density functional theory study on the adsorption mechanism of sulphide gas molecules on α-Fe_2O_3(001) surface, *Inorganics*, 2021, **9**(11), 80.

84 N. I. Oktavianti, *et al.*, Theoretical study of nickel-doped zinc oxide interaction with methylene blue and methyl orange using DFT methods, *Mater. Res. Express*, 2022, **9**(12), 125505.

85 N. I. Oktavianti, *et al.*, Computational study of methylene blue on nickel doped ZnO cluster, in *AIP Conference Proceedings*, AIP Publishing LLC, 2021.

86 C. N. Peter, *et al.*, Theoretical studies of the interfacial charge transfer and the effect of vdW correction on the interaction energy of non-metal doped ZnO and graphene oxide interface, *Theor. Chem. Acc.*, 2018, **137**(6), 75.

87 A. Kausar, Conjugated polymer/graphene oxide nanocomposites – state-of-the-art, *J. Compos. Sci.*, 2021, **5**(11), 292.

88 Y. Guo, *et al.*, Photocatalytic activity enhanced *via* surface hybridization, *Carbon Energy*, 2020, **2**(3), 308–349.

89 S.-K. Park, *et al.*, Structural and conformational studies of *ortho*-, *meta*-, and *para*-methyl red upon proton gain and loss, *Bull. Korean Chem. Soc.*, 2005, **26**(8), 1170–1176.

90 X.-q Wang, *et al.*, Photocatalytic oxidation degradation mechanism study of Methylene Blue dye waste water with GR/iTO2, in *MATEC web of conferences*, EDP Sciences, 2018.

91 L. G. Devi, K. A. Raju and S. G. Kumar, Photodegradation of methyl red by advanced and homogeneous photo-Fenton's processes: a comparative study and kinetic approach, *J. Environ. Monit.*, 2009, **11**(7), 1397–1404.